Received: 4 March 2021 | Revised: 10 June 2021 | Accepted: 28 June 2021

DOI: 10.1002/er.7030

RESEARCH ARTICLE

INTERNATIONAL JOURNAL OF ENERGY RESEARCH WILEY

CNN-based deep learning technique for improved H7 TLI with grid-connected photovoltaic systems

Suganthi Ramasamy[1] | **Maruthupandi Perumal**[2]

[1]Research Scholar, Electrical and Electronics Engineering, Government College of Technology, Coimbatore, India

[2]Department of Electrical and Electronics Engineering, Government College of Technology, Coimbatore, India

Correspondence
Suganthi Ramasamy, Research Scholar, Electrical and Electronics Engineering, Government College of Technology, Coimbatore, India.
Email: rsuganthiphd@gmail.com

Summary

In this article, a three-phase transformerless inverter (TLI) for a solar photovoltaic (PV) system connected to a high-power grid are proposed, which has advantages of better performance and lower cost. The primary concern about the TLI is fluctuations in the common-mode voltage, which impacts switching frequency leakage current and grid interface system. An improved H7 common-mode voltage (CMV) clamped TLI with discontinuous pulse width modulation (DPWM) is designed using a conventional neural network (CNN)-based deep learning approach. In this, a completely minimized leakage current is obtained to avoid CMV transients. The proposed PV-connected improved H7-TLI provides low-loss DC-side decoupling, which further reduces leakage current and isolation of the PV system during off-grid. In addition, the effects of several factors on CNN deep learning performance are explored, including training data size, image resolution, and network configuration. The proposed technique has the potential to be used in a test instrument for intelligent signal analysis or used in an artificial intelligence system. Switching loss is analyzed using proposed and existing H7 inverters under different load conditions. To verify the theoretical explanation, existing H7 inverters is analyzed by MATLAB/Simulink, and the outcomes are tested experimentally. The total harmonic distortion (THD) analysis of proposed and existing topology is analyzed and compared. The THD values of the existing and proposed topology are 3.74% and 3.23%, respectively.

KEYWORDS

conventional neural network, discontinuous pulse width modulation, H7 inverter, PV system, transformerless inverter

1 | INTRODUCTION

Global energy demand is increasing owing to population growth. Renewable energy sources (RESs) play an important role in countering these energy crises. Among all the RESs, photovoltaic (PV) systems have had the generation pattern to increase rapidly in recent years.[1] PV systems have two types of generational systems. The first is a stand-alone system for generating PV power, which is connected directly to the load with or without a battery. The next one is PV generation system with grid-connected mode.[2] Typically, high-power generation systems use a three-phase grid-connected system.[3]

In general, a PV system has two types of grid-connected inverters: grid-connected inverters with a high-frequency (HF) transformer on the DC-side inverter

or a low-frequency (LF) transformer on the AC-side inverter.[4] This increases the voltage to the transformer grid and also provides galvanic isolation at the zero-voltage level, but the main limitation of this system is caused by several alternating states, which minimize the overall performance of the system.[5] This issue may be diminished to the transformerless grid-connected inverter. Despite that, safety obstacles develop according to the leakage current flow between the PV metal frame and the floor.[6]

To prevent this leakage current, several inverter topologies have been proposed. This terrain was mainly classified under galvanic isolation with CMV and galvanic isolation without CMV.[7] In an inverter without a transformer, galvanic isolation is achieved by adding additional switches on the DC or AC side.[8] The extra switches on AC side provide better performance by minimizing switching losses.[9,10]

Today, the performance of photovoltaic (PV) installations is evaluated with monitoring systems, either through the inverter or through the proprietary data acquisition software and hardware control panels.[11] Most of the existing monitoring systems give a simplistic view of energy performance and performance ratio, as more sophisticated dashboards may also alert operators to abnormal performance behavior through online comparisons among expected and measured energy performance. Regarding the expected PV energy production, different prognostic models have been accounted (depending on machine learning strategies, parametrics, and regression methods). These models need the technical details and specifications of the PV system as input characteristics. The manufacturer's data may be unreliable or demonstrate differences based on several factors. To deal with this problem, Firman et al developed methodologies to experimentally decide the peak power of a PV system using monitored measurements of the PV installation.[12] On the contrary, the easiest and most general execution of fault detection is implemented with the inverter on the AC side. Even in the absence of the monitoring system, the inverter may be utilized based on detected grid errors (voltage and frequency deviations) or matrix faults that could be unsafe (arc or ground faults), and thus the inverter may continue to ensure the safety of the installation. Currently, the most famous fault-detection process depends on the imaging process. These imaging processes involve infrared thermography, ultraviolet fluorescence, photoluminescence, and electroluminescence, and offer the capability to inspect an existing power plant and accurately detect a series of faults across the image analysis. Visual inspection is a common technique employed to detect faults during visual evaluation of PV arrays for observing visible faults on PV systems. Although these processes may recognize the entire known faults on PV systems, they are time-consuming and need additional (generally expensive) equipment. Based on the obtained results, the proposed technique offers real-time detection, best operating and maintenance practices with time savings. With the current advancements in the field of artificial intelligence (AI) and rapid advancements in statistic data analysis processes, fault detection and classification of critical infrastructure have grabbed much attention.

The current state of the art in the PV industry for automated recognition and classification of faults refers mainly to the definition of threshold levels for every monitored parameter wherever the comparison of measured value using expected value with defined threshold may give information about the fault condition. These thresholds may be static or dynamic. The benefit of this comparative strategy involves simplicity of execution at a broad range of PV systems, while the drawback involves the requirement of a simulation model. Several developed algorithms detect discrete changes in the performance of individual sensors, rather than correlating measurements from multiple sensors. Lastly, other strategies remove knowledge as obtainable data with machine learning process (like neural networks, fuzzy logic, and expert systems) to decide on fault conditions. The existing literature on data analysis-based methods was utilized for fault detection. Different monitoring processes were utilized to deal with the major system failures and monitoring systems for PV installations. Many current advances are presented in energy monitoring, diagnosis, and forecasting for PV systems. Particularly, fault-detection process depends on data analysis of operational parameters that reached directly the field, and other techniques with AI and data mining were suggested. In addition, Madeti and Singh suggested a comprehensive review of popular fault-detection process for PV systems.[11]

In this study, the diverse sorts of fault-detection process on the DC and AC sides of PV systems were talked about and were addressed. Some authors discussed an evaluation of prognostic and health management tools for the DC side of PV systems. This paper summarized the PV fault detection and diagnosis (FDD) methods utilized on detection and diagnosis of PV faults on the DC side. In addition, the IEA published a report offering a comprehensive set of practical guidelines for analytical monitoring of PV systems. Expanding on its work on the field, the IEA published a report presenting the advanced statistical analysis algorithms utilized for the prediction and detection of faults. Some authors suggested an evaluation of the current state of FDD process of PV systems. Particularly, the types and causes of failures of PV systems were suggested, and the diverse FDD methods were compared based on complexity, ability to detect,

recognize, and locate failures, response time, and application capacity on diverse PV plants. The benefits and limits of the FDD methods were also converse. The aim of this study is to close the knowledge gap in the field of fault diagnosis by giving helpful information on classification methods to recognize the nature of detected faults in the PV system.

1.1 | Objectives and contribution

The objectives and contributions of this study are listed as follows:

1. In the proposed study, the three-phase transformerless inverters (TLIs) for solar PV system connected to a high-power grid are proposed with better performance and lower cost.
2. The main novelty of the proposed work is to get the general optimal solution collected using the proposed topology.
3. The proposed study is useful for solving the optimization problem. An improved H 7 common-mode voltage (CMV) clamped TLI with discontinuous pulse width modulation technique (DPWM) is proposed using a conventional neural network (CNN)-based deep learning (DL) approach. In this, a completely minimized leakage current is obtained to avoid CMV transients.
4. By then, the performance of the proposed scheme is performed on MATLAB/Simulink working platform, and the implementation is evaluated using existing techniques.

The article is organized as follows. Section 2 discusses the related literature studies. Section 3 analyzes the existing H7 inverter with switching states. In Section 4, the proposed H7 TLI topology and its inverter switching pattern are described and along with power losses and temperature coefficient calculation of devices. Section 5 presents the proposed CNN-based DL technique. Section 6 bases on the simulation analysis in existing and proposed topologies. Section 7 describes experimental-based analysis in the existing and proposed topologies. Finally, the conclusion is drawn in Section 8.

2 | RECENT RESEARCH WORK: A BRIEF REVIEW

In the literature, several investigation operations that depend on the transformerless three-phase inverter for grid-connected PV systems (GCPVSs) using various techniques and aspects are available. Some of them reviewed are as follows.

Ahmad and Singh[13] explained that leakage current was an important factor for grid-connected transformerless PV inverters (TLPVs). In general, they were characterized by leakage current reduction systems based on CMV and CMV clamping without galvanic isolation: CMV switches without CMV clamping oscillators and oscillations based on parasitic bonding capacity and topography parameters. For completing the removed leakage current, the CMV should remain constant throughout the inverter operation. Rahimi et al[14] have presented a filter-clamped inverter that was used in TLPV connected to a three-phase. The TLPV inverters were highly well-organized and cost effectual compared with alternatives that rely on HF and LF isolation transformers. On contrary, the TLPV inverters create more leakage current as the isolation transformer was removed. Palanisamy and Vijayakumar[15] implemented a four-wire, three-phase Z-source voltage source inverter (VSI) powered by a transformerless GCPVS and operation by 3D space vector modulation (3D-SVM) technology. In general, leakage current issue was the major drawback of the inverter system without a transformer; this can be controlled and minimized to utilizing the proposed 3D-SVM technique. This proposed system getting DC input source as PV system and peak power was monitored utilizing maximal power point tracking (MPPT) and Perturbation & Observation (P&O) approach, and inverter output VSI was linked to the grid-connected system during coupled inductor.

Zhu and Fei[16] have established a Global Fast Terminal Sliding Mode (GFTSM) adaptive control system employing the fuzzy neural network (FNN) that was introduced single-phase solar PV grid linked without transformer system, mostly an intermediate boost and DC–AC inverter. The MPPT was done in the boost area to get the maximal power as PV line. GFTSM control system was introduced to the H-bridge inverter, thus tracking error among grid reference with inverter output voltage became zero at defined times. FNN was employed to assess system uncertainties in real time because it was difficult to obtain the system uncertainties. Satti and Hasan[17] have implemented a direct prognostic control model for innovative H-bridge multilevel inverter topology that depends on the GCPVS. Direct model predictive control (DMPC) has more benefits than the conventional control approach, together with optimization, the capability for dealing multiple control targets, and direct handling of semiconductor switches rather than the modulator. The maximal energy extraction from the PV system provides optimal flow of current and minimum

total harmonic distortion (THD) and this is the main role of the presented system.

Rahimi et al[18] have suggested that a grid-connected three-phase PV system (called H8) was established for solving the leakage current problem. The alternating current CMV and leakage current create the most important problems in the transformerless GCPVSs. This maximizes the distortion and losses of current applied to the network, in turn creating unwanted radiation. Voltage source full bridge inverters, called B6 type converters, were largely employed for three-phase PV systems. The B6 inverter was susceptible to current leakage, limiting its applications in transformerless GCPVSs. Anurag et al[19] presented an integrated DC–DC converter in terms of transformerless grid connection. A PV inverter that was used to power the PV system was introduced. The grid voltage was intended to preserving high efficiency, but the phase of voltage still falls under the maximum value. A modulation technique was highlighted to reduce the flow of the common method leakage current.

2.1 | Background of research work

The review of recent work shows that the TLI of GCPVS is an important contributing factor. Currently, electricity generation through PV systems has seen the largest raise among other RESs. Furthermore, the inverter must be able to add a defined number of reactive powers addicted to grid, as required using international regulations. PV panels could increase the voltage level and current imbalance; deteriorating harmonic distortion can cause voltage increase. LF transformers are heavy, bulky, and expensive and they diminish system performance owing to loss of power on windings. However, a significant diminution on their size and weight may be reached using HF transformers. It may recover the effectiveness of the system and make them lighter, smaller, and cheaper. Many researchers have pointed out the commercial reason and industrial applications as a major role in DC voltage and current conversion, such as CMV, FNN, MPPT, and DMPC. In the FNN, the system also accepts input information—even imprecise, distorted, and with errors. The major merit of the FNN controllers is the lack of a systematic methodology for their design. The major benefit of the MPC is the fact that it permits the optimization of the present time slot, while keeping future time slots in mind. The MPC requires the repetitive solution of optimal control problems on finite forecast horizon. The MPPT technique has less parameters simple realization and better control and major drawbacks is accuracy sampling is high and computation requirement is large. These above mentioned drawbacks are motivated in the existing systems do this research work.

3 | EXISTING THREE-PHASE H7 INVERTER TOPOLOGY OF PV

The single-phase H-5 inverter topology is used to extent to develop a three-phase H7 topology, which is illustrated in Figure 1. The seventh switch (S_7) provides the isolation among grid and PV through the off-grid voltage.[20,21] CMV variants must remain constant to minimize leakage current. The CMV can be expressed as follows:

$$V_{CMV} = \frac{V_{aN} + V_{bN} + V_{cN}}{3} \tag{1}$$

However, this topology does not provide a current flow path at zero-voltage level.

$$S_7 = S_1\overline{S}_3 + \overline{S}_1 S_5 + S_3\overline{S}_5 \tag{2}$$

Discontinuous PWM technique with seven switching states is proposed to maintain the CMV as a constant, which also reduces the leakage current. Switching pulse pattern of S_7 is a complementary function of switches S_1 to S_6, which is demonstrated in Equation 1. Table 1 presents the switching states and CMV of H7 TLI.

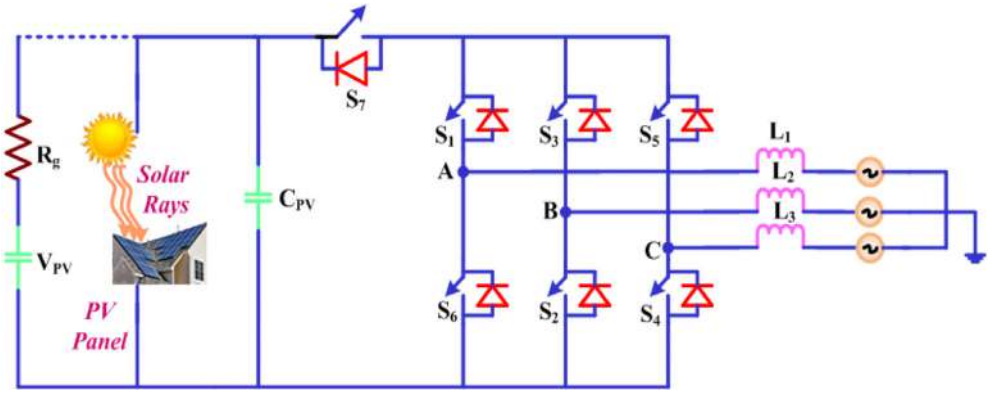

FIGURE 1 Circuit diagram of existing H7 inverter topology

TABLE 1 The switching state of existing H7 transformerless inverter

Switching rate	SW_1	SW_2	SW_3	SW_4	SW_5	SW_6	SW_7	V_{CMV}
V_1	1	1	0	0	0	1	1	$V_{DC/3}$
V_2	1	1	1	0	0	0	1	$2\,V_{DC/3}$
V_3	0	1	1	1	0	0	1	$V_{DC/3}$
V_4	0	0	1	1	1	0	1	$2V_{DC/3}$
V_5	0	0	0	1	1	1	1	$V_{DC/3}$
V_6	1	0	0	0	1	1	1	$2\,V_{DC/3}$
V_0	0	1	0	1	0	1	0	V_{DC}
V_7	1	0	1	0	1	0	0	V_{DC}

During grid injecting period, CMV varies between 2 $V_{DC}/3$ and $V_{DC}/3$. During the off-grid period, CMV becomes $V_{DC.}$ So, the terminal voltage transits between $V_{DC,}$ 2 $V_{DC}/3$, and $V_{DC}/3$ result in high leakage current among PV metal frame and ground. In both H5 and H7 inverters, the output terminals float during off-grid voltage period because of junction capacitance, which leads to the increase in the oscillations in the output current, and the leakage current cannot be fully eliminated.

3.1 | Leakage current and switches junction

In real time, the junction capacity of switch must range from several hundred picofarads to some nanofarads, which may not be disregarded. Leakage current due to high frequency CMV when the inverter changes from switching position to freewheeling position (galvanic isolation or decoupling state), the output voltage of V_{aN}, V_{bN} are based on capacitance switches. Consequently, CMV is vulnerable and adds to leakage current, as it is a major reason of leakage current. For researching the current generation of leakage based on junction capacity, the H7 topology is accepted. The phase and PV modules in the power transmission phase are connected directly by filter inductors. Thus, the result of junction capacity in CMV is very small.[22,23] Moreover, the S_5 and S_4 switches are turned off concurrently in an unstable state. When switch S_3 begins conducting through hidden state, the voltages V_{aN}, V_{bN} may be expressed with KCL,

$$V_{aN} = V_{bn} = \frac{S_2 + S_5}{S_2 + S_5 + S_4} \times V_{PV} \tag{3}$$

The above equation reveals that CMV is stable and equal to $V_{PV/2}$ only if $S_4 = S_2 + S_5$. Unexpectedly, it is not probable on real-time applications. Therefore, junction switches and output filter actuators act as resonant circuits for providing a path of leakage current. To completely diminish the leakage current, the CMV climber line must be galvanized to keep the CMV constant throughout the inverter operation. Typically, the climber branch has real switches (ie, insulated-gate bipolar transistors [IGBTs]) or reactive switches and capacitor, ensuring that the CMV is set to half of input DC connection voltage. Therefore, this study proposed active CMV climbing with H7 topology.

4 | PROPOSED TOPOLOGY

Improved DC-decoupled clamped H7 inverter topology is proposed to remedy the problems in the H7 inverter. The proposed inverter topology and its switching pattern are shown in Figure 2. In this topology, the DC-link capacitor is clamped with active control IGBT switch as $V_{PV/2}$ and $V_{PV/2}$. Switching states and CMV of the proposed topology are shown in Table 2. To analyze the switching pattern, switching frequency is drawn for 500 $H_{Z.}$[24-26] To analyze the CMV, the switching pattern is categorized as follows. Switching pulse for S_8 is derived from Equation (2), which becomes

$$S_8 = \overline{S}_7 = \overline{S}_1 S_3 + \overline{S}_5 S_1 + S_5 \overline{S}_3 \tag{4}$$

In Equation (5), the switching pulse of the eighth switch is the complementary function of the seventh switch.

Case I. Switching Strategy A

The proposed H7 TLI switching pattern is shown in Figure 3. The switching pattern during odd vectors (V_1, V_3, V_5) either one of the upper switches conducts consequences with two lower switches with switching frequency, switch S_7 is continuously on with high frequency and S_8 is OFF, then CMV becomes $V_{DC/3}$.

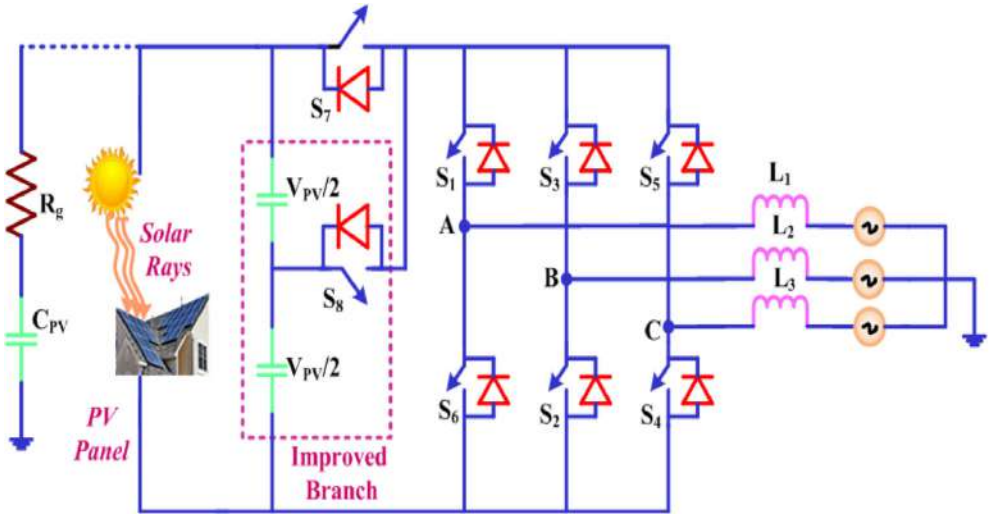

FIGURE 2 Proposed H7 transformerless inverter

TABLE 2 Switching state of proposed H7 TLI

Switching rate	SW_1	SW_2	SW_3	SW_4	SW_5	SW_6	SW_7	SW_8	V_{CMV}
V_1	1	1	0	0	0	1	1	0	$V_{DC/3}$
V_2	1	1	1	0	0	0	1	0	$2\,V_{DC/3}$
V_3	0	1	1	1	0	0	1	0	$V_{DC/3}$
V_4	0	0	1	1	1	0	1	0	$2V_{DC/3}$
V_5	0	0	0	1	1	1	1	0	$V_{DC/3}$
V_6	1	0	0	0	1	1	1	0	$2\,V_{DC/3}$
V_0	0	1	0	1	0	1	0	1	Undefined
V_7	1	0	1	0	1	0	0	1	Undefined

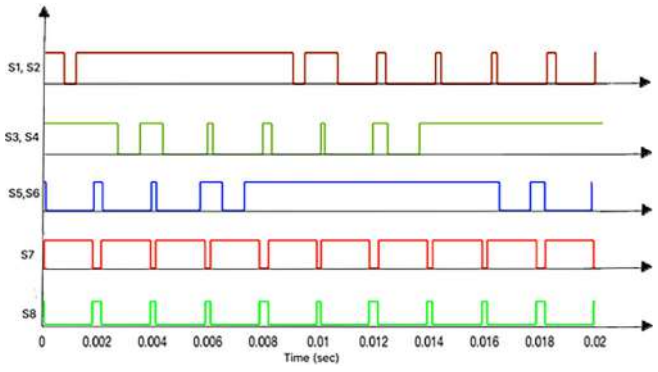

FIGURE 3 Proposed H7 transformerless inverter switching pattern

Case II. Switching strategy B

Switching pattern during even vectors (V_2, V_4, V_6): any two of the upper switches conducts sequences with one lower switch with switching frequency; switch S_7 is continuously on with HF and S_8 is OFF, then CMV becomes $2V_{DC/3}$.

Case III. Switching strategy C

Switching pattern through the freewheeling period (V_0, V_7): all upper switches or lower switches conduct with switching frequency; switch S7 becomes OFF, switch S8 conducts with HF, and then CMV becomes $V_{DC/3}$ or $2V_{DC/3}$ depending on the previous state, so it becomes undefined. Unlike the existing H7 topology, the proposed topology with off-grid period and the clamping switch S_8 starts, conducts, and creates the current path for flow leakage current. A CMV fluctuation gets reduced, so the CMV varies between $V_{DC/3}$and $2V_{DC/3.}$ However, we cannot keep the CMV constant without any fluctuations. To keep the CMV constant, we need additional switches and modified switching topology, which leads to complications in the circuit and increases the system cost.

4.1 | Mathematical modeling of PV

The most essential component of PV system implies the solar cell that involves the conversion of solar energy into electrical energy.[27] PV generation is defined as the process of generating voltage or electricity in a PV cell when exposed to sunlight. A solar cell consists of materials such as silicon that absorbs light. Energy knocks electrons loosely and they flow generously, making a dissimilarity in the voltage, generating electrical energy. PV establishment is ground-mounted, rooftop-mounted, wall-mounted, or floating. Figure 4 presents that circuit diagram for the PV module. The flow of photocurrent (I_{PH}) is performed by load connected toward the output terminal cell. A source current parallel to the diode is the ideal equivalent circuit of solar cell. The circuit output terminals have been connected through load. The equation of voltage–current of solar cell is given as follows:

$$I_{pv} = I_{PH} - I_{DR}\left(e^{\frac{qV_{pv}}{Kt}} - 1\right) \quad (5)$$

Here, the photocurrent is represented as I_{PH}, diode reverse saturation current as I_{DR}, the electron charge as q, the Boltzmann constant as K, and the temperature of the cell as t.

The solar cell output power is computed as follows:

$$P_{out} = V_{pv} \times I_{pv} \quad (6)$$

Here, P_{out} indicates the solar cell output power, V_{pv} indicates the solar cell operating voltage, and I_{pv} implies the solar cell output current.

FIGURE 4 Flowchart for proposed CNN-based deep learning technique

4.1.1 | Available solar power

The output power from SPV cell is established via the count of solar radiation in specific site. The PV series hourly output is expressed as,

$$P_{PV}^{t} = f_{PV} y_{PV} \left(\frac{I_t}{I_s}\right) \tag{7}$$

Here, P_{PV}^{t} is represented by the power obtained by the PV panel, f_{PV} is specified as the PV berating factor, y_{PV} is indicated as the array capacity of PV, and I_t is denoted as the global solar radiation in PV sequence. The eliminating factor signifies PV. A measuring factor (usually ≤100%) is used to calculate the losses caused by high ambient temperature, various functioning voltages, and soil of the panels in the series output.

4.2 | Discontinuous pulse width modulation for H7 level inverter

During the conditions of alternating solar radiation or fluctuating phase voltage, the inverter voltage should be controlled for preserving the current flow to the phase through sinusoidal phase current I_g. The inverter voltage must be controlled by the reference magnitude or by the modulation index $MI = A_{\mathrm{Ref}}/2A_{cr}$ of proposed three-phase H7 level PV TLI.[28,29] For the H7 TLI, a novel double-reference carrier phase-shifted PWM has been evolved with the CNN system. M represents the carrier signal, and it has H7 TLI modules. The PWM phase-shifted from 360°/M. Two reference signals of each magnitude A_{Ref} among the similar phase are utilized, but it consists of a negative offset voltage similar to carrier magnitude. For each inverter module two tips for comparing PWM excitation pulses are adopted. For the H7 TLI model, two hybrid inverter modules are linked on layers so that two carrier signals are phase-shifted with 360°/2. Each inverter module requires two reference signals, $V_{\mathrm{Ref}1}$ and $V_{\mathrm{Ref}2}$, which are identical in phase and magnitude, except that $V_{\mathrm{Ref}2}$ consists of negative offset value with the carrier signal maximum amplitude A_{cr}.

4.3 | Power losses and thermal module

Losses in the inverter are inevitable, which produce heat in the devices and affect the reliability. Power losses are categorized as semiconductor switches losses and losses in damping resistors and DC-link capacitors.[30] Here, we focus on switches losses and losses due to the damping resistor. The calculation of the power losses of the switches is described as follows. The device specifications are given in Table 4.

4.3.1 | Calculation of IGBT losses

The losses in the IGBT can be grouped into conduction and switching loss. The total power loss switch is

$$P_{IGBT} = P_{cond.IGBT} + P_{SW.IGBT} \tag{8}$$

Conduction losses of device changes according to collector current and the voltage drop across the switch during one state.

$$P_{cond.IGBT} = V_{ce(sat)} \times I_C \tag{9}$$

Switching loss of the IGBT depends on the ON and OFF period of energy losses, frequency, DC link, and DC-link voltage on datasheet.

$$P_{SW.IGBT} = P_{ON.IGBT} + P_{OFF.IGBT} \tag{10}$$

$$P_{SW.IGBT} = E_{ON} \times f \times \frac{V_{cc}}{V_{cc.datasheet}} + E_{OFF} \times f \times \frac{V_{cc}}{V_{cc.datasheet}} \tag{11}$$

$$P_{SW.IGBT} = (E_{ON} + E_{OFF}) \times f \times \frac{V_{cc}}{V_{cc.datasheet}} \tag{12}$$

4.3.2 | Diode loss calculation

Conducting loss of the diode can be analyzed using

$$P_{cond.Diode} = V_{ce(Sat)} \times I_F \tag{13}$$

Switching losses of the diode can be analyzed using

$$P_{SW.Diode} = P_{ON.Diode} + P_{OFF.Diode} \tag{14}$$

$$P_{OFF.Diode} = \frac{1}{8} \times T_{rr} \times I_{rr} \times V_R \times f \tag{15}$$

The DC bus capacitance losses become

$$P_R = R \times i^2 \tag{16}$$

The conducting loss and switching loss of existing and proposed topology are compared, in which, the losses observed in switches S_1 to S_6 are the same, but they lower than the losses observed in switch S_7 and S_8. The switches create an increase

in power losses, which results in increasing junction temperature. There is a limit in the manufacture datasheet to provide the maximum junction temperature. The junction temperature depends on the internal resistances of the devices and the losses of switches, which can be derived as

$$T_j = R_{th(s-a)} \times P + R_{th(c-s)} \times P + R_{th(j-c)} \times P + T_a \quad (17)$$

here $T_j, R_{th}(s-a), R_{th(c-s)}, R_{th(j-c)}, P, T_a$ implies junction temperature, heat sink thermal impedance, heat sink with circuit element thermal impedance, circuit element with heat sink thermal impedance, and ambient temperature, respectively. The junction temperature of the switches S_1 to S_8 is less than that of the switches S_7 and S_8.

4.3.3 | Power factor correction

The proposed topology has the capability to achieve the power factor correction (PFC) mode of operation from active filter appliance. The equation is given as follows[31]:

$$\eta = \frac{P_o}{P_o + P_{loss}} \times 100 \quad (18)$$

where P_{loss} is the power loss and P_o is the output power.

4.4 | Closed-loop control of solar PV-based H7 transformerless inverter

To get power from the solar PV panel to the application phase, the inverter current (phase current) must be controlled so that the individual DC link voltages are uniform and the total DC connection voltage (total inverter's MVDC) $\sqrt{2}$ times of V_g should be many times more in the case of solar radiation.[32] For a nontransformer inverter through Z-number hybrid modules, the relationship among phase voltage (V_g) and its DC connection voltage (V_{dc}) may be articulated as follows,

$$ZV_{dc} > \sqrt{2}V_g \quad (19)$$

Here, Z is the modulation index; the reference voltages without a transformer inverter may be tuned by a closed-loop current controller. The demonstration of grid-connected three phase improved H7 TLI topology considers H-5 inverter modulation index is 2 and connected to a phase utilizing step-up transformer with a ratio of 1:2. Thus, for electricity to flow toward grid, DC connection voltage (V_{dc}) of all hybrid inverter module must be equal to Equation (20)

$$V_{dc} > \left(V_g / 2\sqrt{2}\right) \quad (20)$$

DC-connected PV systems help to remove maximal power by controlling duty ratio of converter switches. The series output voltage (V_{PV}) must be maintained.

The adopted control scheme for the H7 TLI topology fulfills the following objectives,

- Under different weather conditions, the maximum PV independent control of each DC link voltage to ensure power extraction.
- The proposed H7 TLI is close to the sinusoidal with low harmonics and phase-induced current and power factor is unity.
- Constant operations of the inverter even when in fluctuating grid voltage condition.

4.5 | Voltage control loop of solar PV-based H7 transformerless inverter

Additionally, the DC-link voltage controller and individual DC-link voltage regulators are employed for ensuring equivalent capacitor voltages.[33] Since PV energy varies directly through the level of solar illumination, when the random positions of the PV panels are almost identical, practically, the equal operating point may be assumed; the duty ratio values are S1 and S2. The radiation level is slightly dissimilar for PV panels, the corresponding values of solar energy and therefore S1 and S2 and reference DC connection voltages. Although, for preserving the H7 voltage level TLI topology, the DC connection voltages must be preserved uniformly, evolving an appropriate compensation mechanism outside the scope of current operation.

5 | PROPOSED CONVENTIONAL NEURAL NETWORK–BASED DEEP LEARNING TECHNIQUE

In this article, the CNN-based DL, as a fast-growing, sophisticated field of research, is proposed to improve the H7 CMV clamped TLI with DPWMT using a completely minimized leakage current obtained by avoiding CMV transients. The CNN-based DL specializes in computer vision, natural language processing, bio-informatics, and many other scientific disciplines, where traditional ML methods face obstacles or rely heavily on some experience-based knowledge/skills. The most attractive benefits of DL are that it eliminates manual feature engineering. Instead to extract or learn automation features from data.

5.1 | Process of CNN-based DL technique

Compared to the normal neural network, CNN has two types of layers: convolution and pooling layer. A convolution layer has feature maps of existing layer from inputs and performs two-dimensional transition operations among inputs and the set of learnable filters.[34,35]

$$X_N = f\left(\sum_M W_N^M * X^M + B_N\right) \tag{21}$$

where X_N is the N^{th} feature maps, W_N^M is represents that are involved in the convolution operators *, B_N represents the bias value that is equivalent with every feature map. The scattered connection of the convolution layer permits neurons to be connected to local area of input scale that importantly minimizes the number of parameters on sample. This connection method allows CNNs to accept inputs by large dimensions that is infeasible with normal neural networks. It is a nonlinear bottom model function, which integrates a lower number of connection units in a feature map, typically increasing the 2x2 region values with the conversion progression of 2 that converts the model to a smaller translation of the entries. This may lead to CNN that can achieve great success. Besides, the terminal of CNN-based models has usually several fully connected layers (also named dense layers). Those layers are similar to the layers on normal neural networks, wherever the neurons are fully integrated with each process of existing layer and perform a matrix multiplication. In addition, to combine multiple layers, CNN uses a number of new features for enhancing efficiency in classification accuracy and training capability. A saturated execution function is used to replace rectified linear units, derived traditional saturated functions,

$$F(X) = \tanh(X) or F(X) = (1 + e^{-x})^{-1} \tag{22}$$

Another feature is the introduction of "dropout" as a regulatory mechanism to prevent neurons from coinciding via decreasing co-adaptation. Theoretically, this sets the output of the hidden neuron through probability 0.5 toward zero, forcing a network for learning stronger characteristics to common.

5.2 | Data conversion

Conventional Neural Network (CNN) based Deep Learning (DL) is intended to CMV H7 topology and leakage current is an important task. Considering the problem of modulation classification on communication systems wherever difficult model points of modulated signals are obtainable, data transfer is necessary for reducing the gap among two types of data. Thus, the proposed system helps to convert complex model points in a galaxy to use CNN-based DL models. In contrast, the larger selected area results in higher resolution of the CMV, which leads to the rapid development of the computational problem when training a deep network.

5.3 | Network configuration

For facilitating DL network configurations based on CNN, the BLVC reference CaffeNet model is taken and slightly modified for best efficiency and rapid learning speeds. Additionally, various parameters in solver settings such learning rate gamma (γ) and step size are used for best classification performance and training efficiency.

5.4 | Implementation

The CNN configuration may be established at various sources. For most applications, such network variants have been utilized for image analysis. It is utilized for processing the identification of CMV voltage and leakage current. The structure of CNN has several layers.[36,37] The layer descriptions are as follows.

***Step 1*: Input layer**
This layer arrives at the input from proposed H7 topology of CMV voltage and leakage current. It is a process based on time.

***Step 2*: Convolution layer**
The convolutional layer is made up of conventional kernel set in which every neuron functions. This layer handles "convolution filtering" of input data for extracting significant characteristics as data and propagates the information during subsequent layers. The convolution operation may be expressed as follows:

$$f_l^k(p,q) = \sum_c \sum_{x,y} I_g(x,y).e_l^k(u,v) \tag{23}$$

Here, $I_g(x,y)$ is the input parameter of grid current tensor I_g. The input parameter is multiplied by $e_l^k(u,v)$ index of k^{th} convolutional kernel e_l^k of first layer. Then, the output feature map k^{th} convolution function is expressed as follow,

$$F_l^k = \left[f_l^k(1,1),...f_l^k(p,q),...f_l^k(P,Q)\right] \quad (24)$$

In the CNN-based DL, each transition kernel denotes a feature type, for example, temporal variance nature, the sharp edges on data, and so on. In the network, large number of kernels can be employed, and kernel weights have been arbitrarily initialized. Due to initial convolution layer, a dimension filter framework is used.

***Step 3*: Rectified linear units (ReLU) layer**

This layer executes the threshold function dependent on nonlinear endpoint mapping functions.

$$Max(0,s) = \begin{cases} 0 & if\, s < 0 \\ s & Otherwise \end{cases} \quad (25)$$

***Step 4*: Pooling layer**

This layer is the diminution of the leakage current. Maximizing is one of the most famous systems of function. Average and L_2 norms are also used. A change is made when changing the easy pooling function. This is performed by simply initiating another convolution layer, other than dissimilar slide on the time axis through the kernel change.

***Step 5*: Fully connected layer**

This layer is equal to CNN, and as the name implies, every neuron in this layer is linked with entire functions of the previous layer. It is worth noting that this layer really does the sorting job, while the previous layers do present the learning. Such layers may be done *N* times based on the degree of accuracy needed.

6 | SIMULATION RESULTS AND DISCUSSION

Simulations were done using MATLAB/Simulink to confirm the process and leakage current and CMV performance of the existing and proposed inverters the same as the parameters utilized. The PV array has two series-connected Sanyo HIP-225 HDE1 modules. To verify the proposed topology of H7 TLI with DL CNN technique, two case studies were analyzed. Both the case studies were carried out with the closed-loop control derived equation. Here, three-phase voltage $+V_{PV}, -V_{PV}$ is generated during bipolar modulation, which provides high core losses. However, it produces stable CMV; therefore, the leakage current is minimum. The PWM system is employed to solve leakage current issues. Moreover, the performance of the bipolar PWM inverter is less compared with the unipolar PWM inverter due to the large losses in the core and the switching losses of the filter actuators. Therefore, several inverter topologies have been established that have the benefits of unipolar and bipolar modulation systems for maximum performance and minimum leakage current use. This is classified primarily depends on the leakage current minimization approaches: galvanic isolation with no CMV clamped and with CMV clamped.

CMV switches are based on climbing oscillations based on parasitic parameters of junction capacity and topology. To reduce leakage current, the CMV should be stable all over inverter operation. Furthermore, the inverter should be capable for delivering some number of reactive powers in phase as required through international regulations. Therefore, this topology is filled with an additional common-mode filter (CMF) that puts a burden on the cost and power density of inverters. Here, the CMV–CNN excitation leakage current minimization topology is proposed that can remove leakage current with exerting reactive power in phase. The proposed CMV–CNN constant across all TLI operations and decreased the additional CMF requirement. Furthermore, the THD analysis of proposed method is performed at different levels of solar radiation (100-1000 W/m^2), and the outcomes are obtained in a certain range.

The simulation results for this existing topology are shown in Figures 5 and 6. DPWM technique is applied for both the existing and proposed topology. Figure 5 illustrates the grid voltage of existing topology. Figure 6 shows the grid current of existing topology. Gird voltage and injecting grid current are measured after using line filter inductor. The CMV varies between 200 and 600 V. The injected grid current THD 3.74% and leakage current RMS value denotes 180 mA. Simulation results of existing topology of CMV and leakage current (I leak) are shown on Figure 7. The CMV voltage of existing topology is demonstrated in Figure 7A. Leakage current of existing topology is shown in Figure 7B.

Figure 8 shows the simulation outcomes for the proposed seven-switch topology with DL CNN of grid current and grid voltage. Figure 8A illustrates the grid voltage of proposed topology. Figure 8B shows the

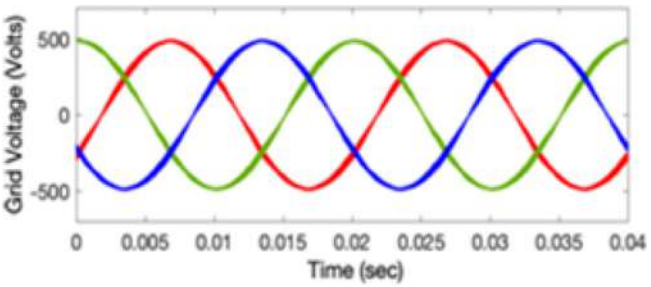

FIGURE 5 Simulation results of existing topology: grid voltage

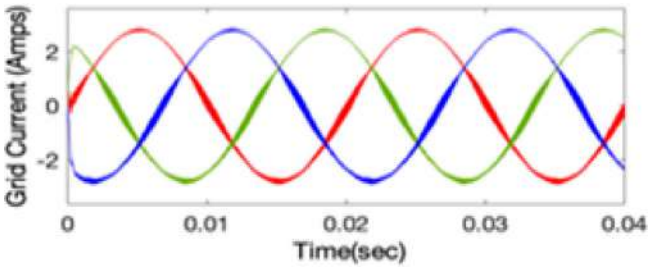

FIGURE 6 Simulation results of existing topology: grid current

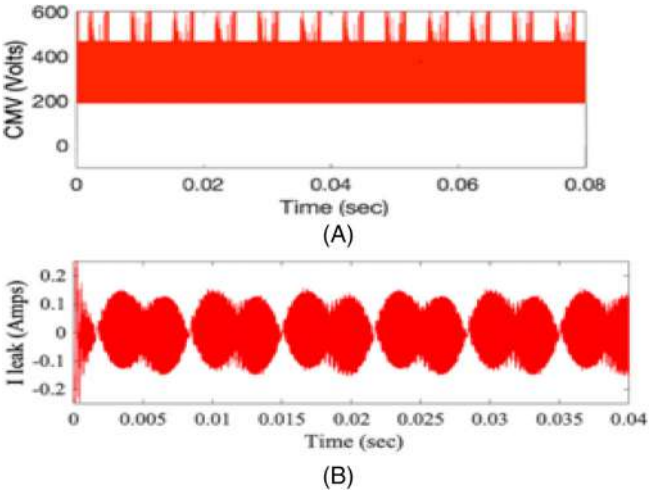

FIGURE 7 Simulation outcomes of existing topology: A, common-mode voltage (CMV) and B, leakage current (I leak)

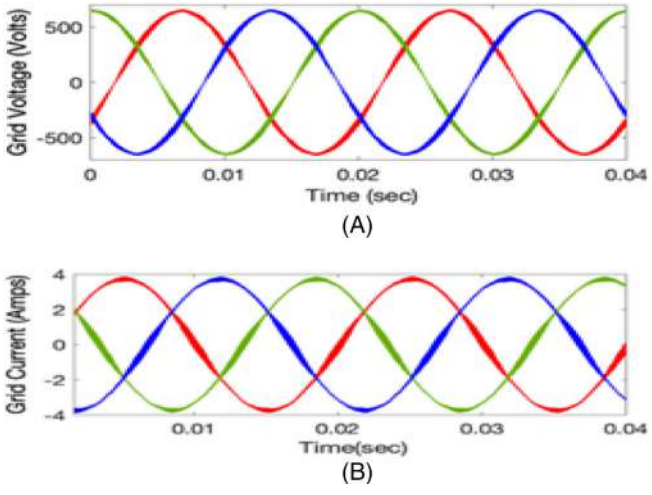

FIGURE 8 Simulation outcomes of proposed topology: A, grid voltage and B, grid current

grid current of proposed topology. Simulation results of existing topology of CMV and leakage current (I leak) are shown in Figure 9. The CMV voltage of existing topology is shown in Figure 9A. The leakage current of the

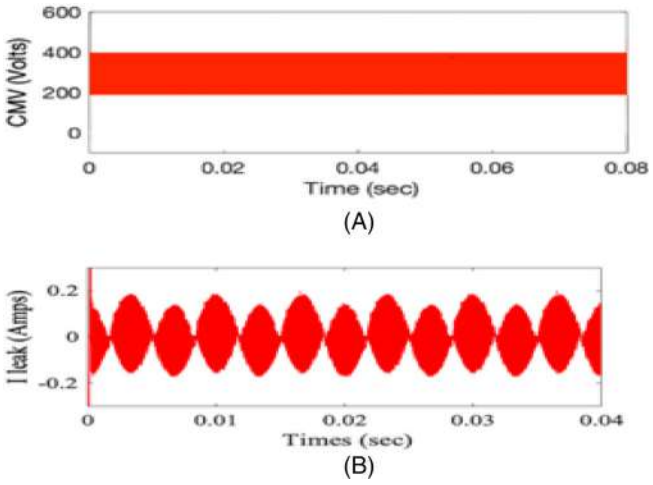

FIGURE 9 Simulation outcomes of proposed topology A, common-mode voltage (CMV) and B, leakage current (I leak)

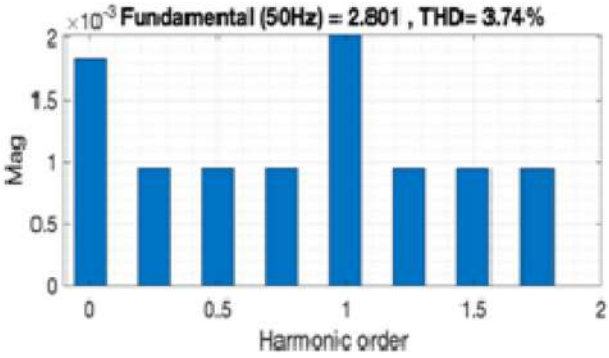

FIGURE 10 Simulation of THD results in existing topology

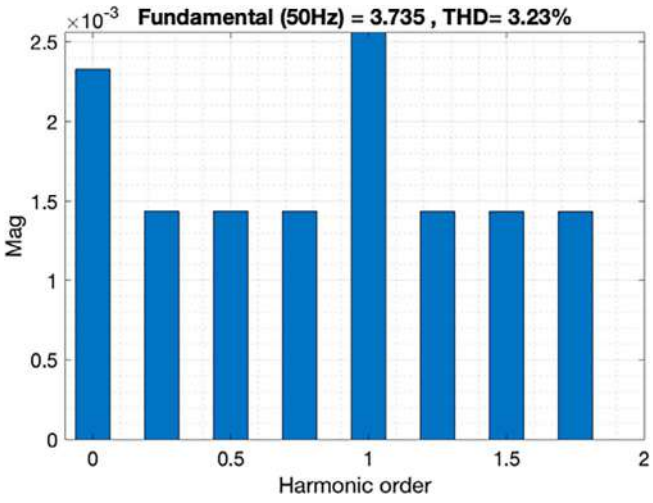

FIGURE 11 Simulation of THD results in proposed topology

existing topology is shown in Figure 9B. Figure 10 shows the THD of existing inverter topology. Figure 11 depicts the THD of proposed topology. Figure 11 illustrates the

grid current THD as 3.23%. The stray capacitor voltage differences are minimized between 200 and 400 V in seven-switch inverter topology. The leakage current RMS value of 120 mA for this Case is less than allowable 300 mA mentioned VDE 0126-1-1, standard that outcomes at very low leakage current in comparison with existing H7 topology with the CNN technique. Figure 12 shows the proposed topology of conduction loss of devices. Figure 13 depicts the proposed topology of switching loss of devices. According to simulation

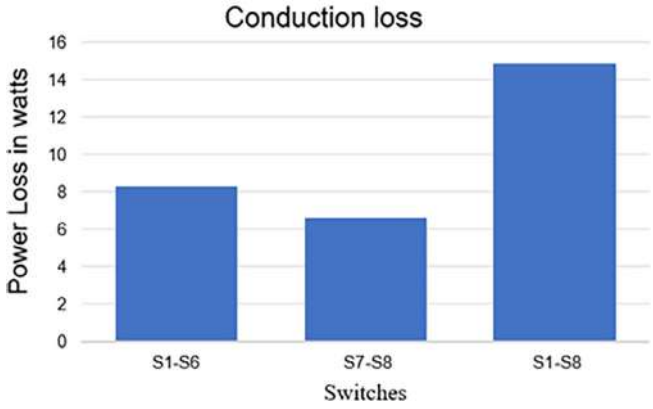

FIGURE 12 Proposed topology of conduction loss of devices

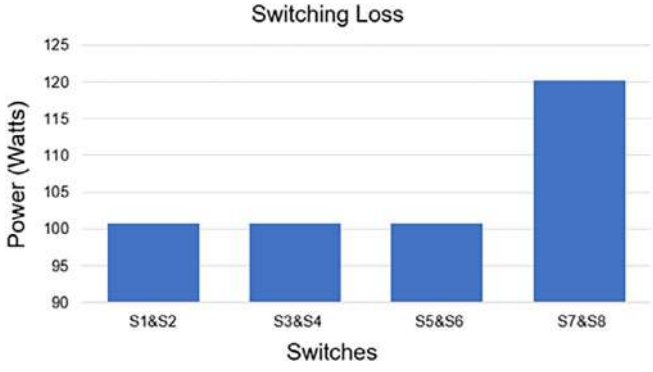

FIGURE 13 Proposed topology of switching loss of devices

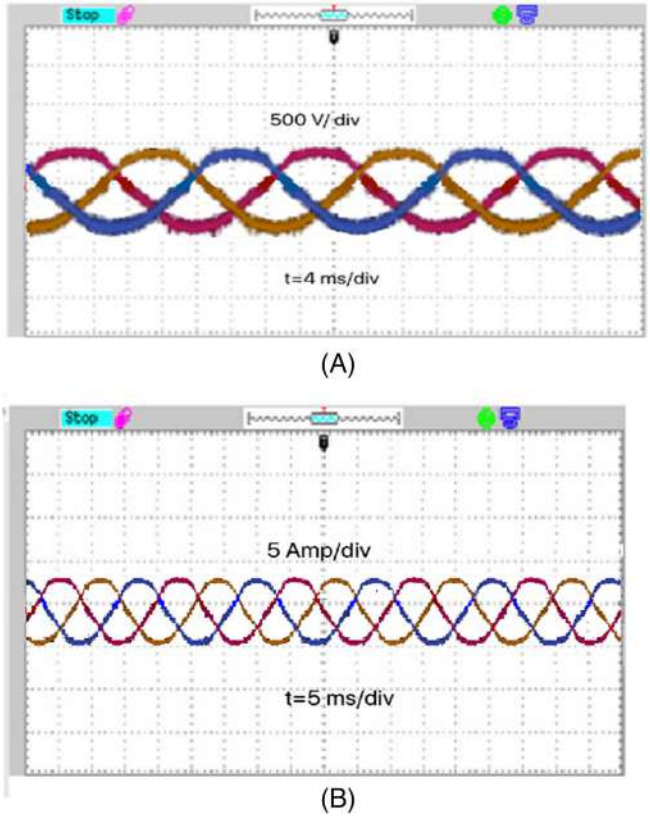

FIGURE 15 Experimental outcomes of existing topology: A, grid voltage and B, grid current

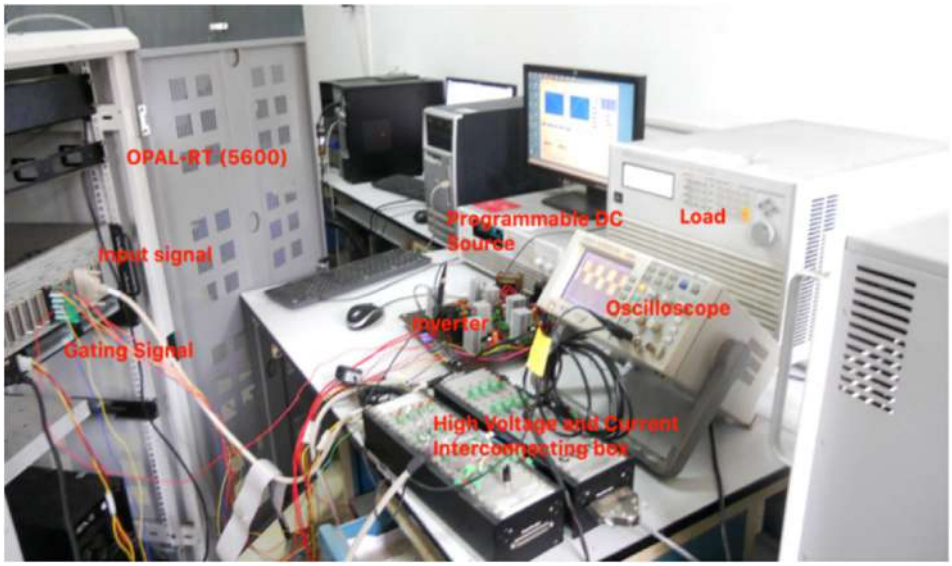

FIGURE 14 Hardware experimental test setup

waveforms, the linearity present in grid voltage and grid current using proposed improved H7 topology with deep learning CNN technique gives better solution than the existing topology.

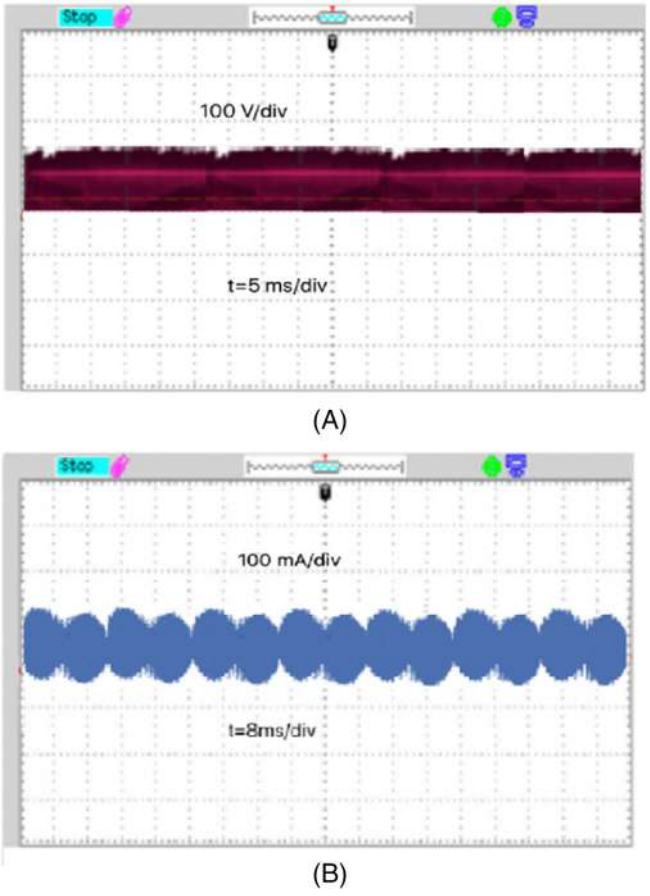

FIGURE 16 Experimental outcomes of existing topology: A, CMV and B, leakage current (I leak)

7 | EXPERIMENTAL RESULTS AND DISCUSSION

For authenticating the simulation outcomes for existing H7 and experimentally proposed H7, the three-phase universal inverter was developed using CNN's DL technique.

7.1 | Implementation of DSP

Digital signal processing algorithm (DSP) is an exact, step-by-step process of mathematical calculations intended for manipulating digital signals. The DSP algorithm is a set of computations intended for manipulating digital audio.

The experimental setup developed for TLI is shown in Figure 7. DC-link voltage is obtained from PV array simulator. Control algorithm the inverter is developed from OPALRT real-time digital simulator.

The stray capacitance load is connected at DC-link positive and negative terminal. The ground resistance is connected in series among stray capacitance. AC supply gives the reference main voltage of 415 V at frequency of 50 Hz to use on controller. Figure 14 shows the overall hardware experimental setup of a proposed topology. The scope scale value is 2-20 seconds.

Experimental CMV characteristics waveforms of H7 and H7 TLI are shown in the waveform. These waveforms are almost similar to the simulation results. The experimental result of existing topology of grid voltage and current is shown in Figure 15A,B. The unipolar output grid voltage and injected grid current existing topology waveforms of CMV voltage are shown in Figure 16A and Leakage current waveform of H7 TLI is

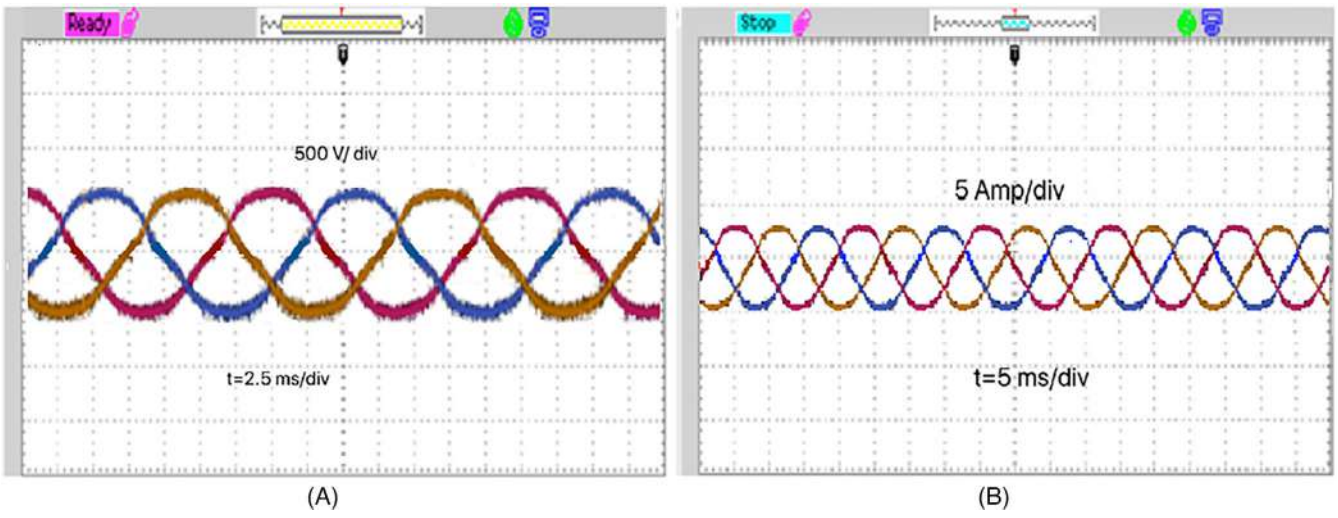

FIGURE 17 Experimental outcomes of proposed topology: A, grid voltage and B, grid current

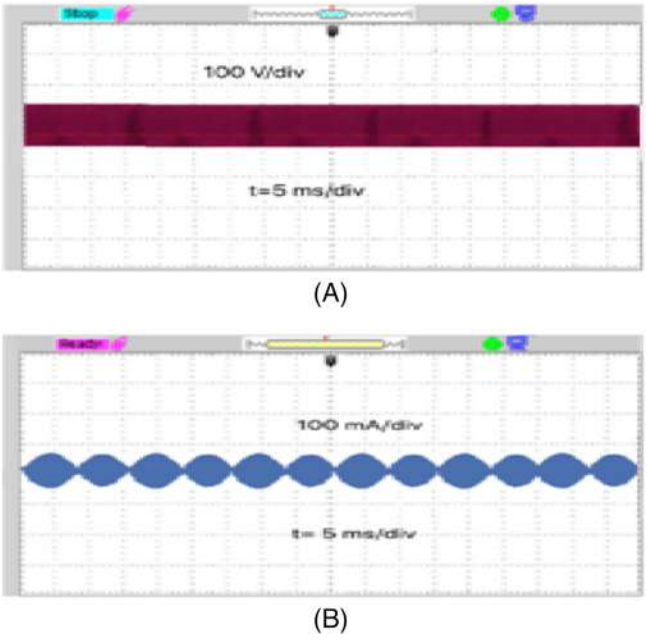

FIGURE 18 Experimental results of proposed topology: A, CMV and B, leakage current (I leak)

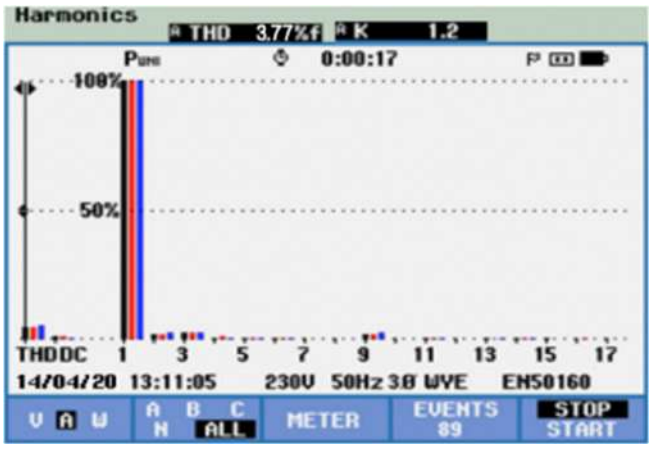

FIGURE 19 Experimental outcomes of THD in existing topology

demonstrated in Figure 16B. The CMV clamping inverter produces less leakage current devoid of CMV clamp inverter. This is because the HF component cannot be completely clamped without the CMV clamping inverter. Same simulation parameters are used for the experimental setup at the standard test condition of the PV panel. The entire control algorithm of DL CNN technique is implemented in SPARTAN 6 family FPGA XG6SLX9, with dead time = 2.2 μs. MSOX3014 A is used for inverter output voltage, currents, leakage current, and common-mode voltages. The experimental outcomes of grid voltage and current of proposed topology are shown in

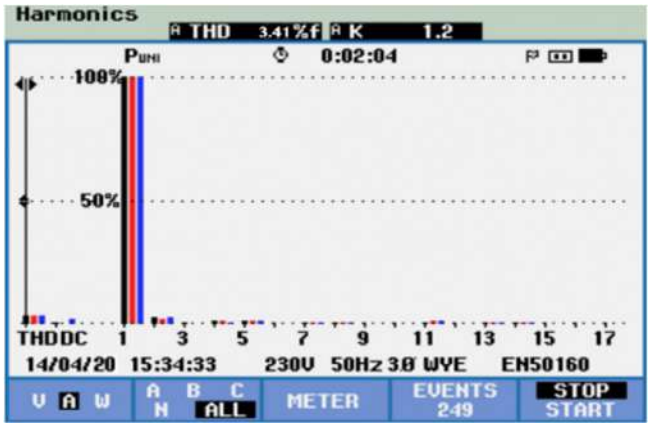

FIGURE 20 Experimental outcomes of THD in proposed topology

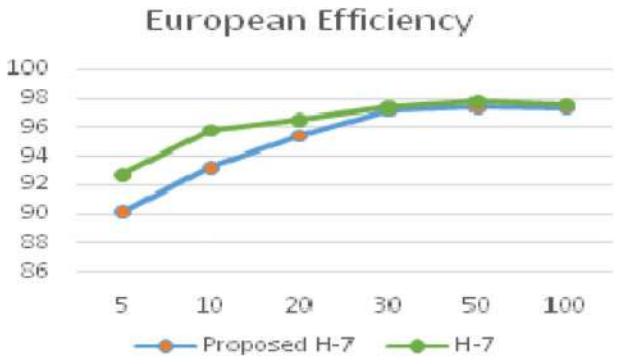

FIGURE 21 Measured efficiency of H7 and improved H7 inverter

TABLE 3 Technical description of CMV

Parameters	Ranges
Grid frequency	50 Hz
PWM carrier frequency	16 kHz
Normal power (P)	1000 W
DC-link voltage	700 V
Stray capacitance (CPV)	220 nf
Ground resistance (RG)	11 Ω
Load resistance (RL)	100 Ω
DC-link capacitance (CDC)	2 mF
Filter inductor (lf)	5 mF
Modulation index	0.95

Figure 17A,B. Harmonics orders are measured by FLUKE 343 B series harmonic analyzer. The experimental result of proposed topology of CMV demonstrated at Figure 18A. The inverter output voltage of H7 with improved H7 TLI unipolar. The experimental results of the proposed topology of leakage current are depicted in

Figure 18B. RMS leakage currents of the H7 and improved H7 inverters are 180 and 120 mA. Leakage current of 180 mA is much higher than the proposed H7 inverter. As compared to H7 inverter, the improved H7 inverter produces much lower leakage current, and at the same time, the CMV fluctuations also get reduced. Common voltage variation is the main factor for leakage current of the inverter. Figure 19 shows the FFT analysis of existing H7 inverter, and Figure 20 depicts the proposed topology of improved H7 inverter topology, respectively. THD has also got reduced to the reasonable limit in proposed topology. So, the experimental results prove that the improved H7 inverter topology with discontinuous PWM technique enhances the overall performance of TLI topology based on output grid voltage, CMV variations, and grid current harmonic spectrum. This portrays that proposed topology is applicable for tri-phase GCPVS without the transformer. The output results among experiment and simulation outcomes under ideal conditions showed very low variations, which depict that the experimental results are on par with simulated results.

The European performance was measured for existing and improved inverters with equal input power (2 kW). Full load efficiency is 97.6% for the existing inverter topology and 97.32% for the improved inverter topology; the measured performance is somewhat less at improved H7 inverter compared the proposed H7 TLI due to additional switch, which is the drawback of this topology; Equation (26) represents the European efficiency. Figure 21 shows the comparative analysis of European efficiency for H7 and improved H7 TLI with advanced DL CNN technique.

$$\eta_{EU} = 0.03\eta_{5\%} + 0.06\eta_{10\%} + 0.13\eta_{20\%} + 0.10\eta_{30\%} + 0.48\eta_{50\%} + 0.2\eta_{100\%}..... \quad (26)$$

Table 1 shows the switching state of existing H7 TLI. Table 2 illustrates the switching state of proposed H7 TLI. The PV array has two series-connected Sanyo HIP-225 HDE1 modules, whose technical specifications are mentioned in Table 3. Table 4 depicts the parameter for loss analysis. Efficiency comparison of proposed, HERIC, H7, H6, and H5 topology is shown in Table 5. The proposed

TABLE 4 Parameter for loss analysis

Parameters/Specifications	Value
IGBT switch	IRGP30B120KD-EP, 1200 V, 25 A
Grid frequency	50 Hz
IGBT-saturation	2.28 V
IGBT-forward	5 V
Junction temperature T_j (max)	125°C
Turn-ON switching loss @ 600 V	1066 μJ
Turn-OFF switching loss @ 600 V	1493 μJ
Calibration factor of P_{cond}-IGBT	1
Calibration factor of $P_{SW\text{-}IGBT}$	1

TABLE 5 Efficiency comparison of proposed, HERIC, H7, H6, and H5 topologies

Solution techniques	Efficiency (%)
H5	87.0913%
H6	89%
H7	96.0019%
HERIC	95.1083%
Proposed	99.143%

TABLE 6 Comparison between simulation and experimental results

Parameter	Proposed topology	Transformerless inverter[38]	Switched capacitor-based inverter[13]	MLI inverter[39]
RMS voltage		230 V	230 V	110 V
Topology	Three-phase improved H7 transformer less inverter	1 phase, H5	Switched capacitor-based inverter	1 phase, multilevel
Control technique implemented	Discontinues pulse width modulation technique (DPWM) using conventional neural network (CNN)-based deep learning approach	ANFIS	—	Vector control
Voltage THD	—	2.13% (Linear full load)	<4%	2.5%
Efficiency	99.143%	98.5%	>85%	97.5%

TABLE 7 Line and load regulation of proposed and existing topology

Line regulation (%V)	H5	0.01
	H6	0.02
	H7	0.04
	HERIC	0.07
	Proposed	0.15
Load regulation (%V)	H5	0.1
	H6	0.5
	H7	0.3
	HERIC	0.7
	Proposed	1.5

technique efficiency is optimal than the other existing topologies. Table 6 shows the comparison among simulation and experimental outcomes. Line and load regulation of proposed and existing topology are shown in Table 7.

8 | CONCLUSION

In this article, a tri-phase improved H7 inverter with DPWM for GCPVSs without the transformer to reduce the leakage current using CNN-based DL is proposed. The performance analysis and simulations are carried out on the MATLAB/Simulink platform of existing H7 inverter and improved H7 inverter topologies. Owing to the high leakage current, the H7 conventional three-phase inverter is not an appropriate choice for transformerless GCPVSs. The improved H7 clamping inverter topology proposed with DPWM topology isolates the PV field from the grid through off-grid period and creates the current flow path of leakage current. Hence, the leakage current result is minimized to low value and complies with the international standard VDE 012-1-1. As per simulation, the leakage current in improve H7 inverter is found to be 120 mA, which is 26% lower than existing conventional H7 inverter topology. The DPWM helps to diminish the leakage current in proposed H7 inverter system, which resulted in improved voltage linearity and output current THD as compared with conventional existing H7 inverter. Based on leakage current and injecting grid current THD, experimental outcome ensures that the improved H7 inverter topology on three-phase inverter without transformer provides better performance. Power loss calculations of switching devices are made. Proposed improved H7 inverter topology produces high power loss compared to existing H7 topology due to additional switches. The efficiency of both the inverters is calculated at different load conditions.

For completing this proposed work, a PV system is connected to the grid with smart grid functionality; there is a huge designing required in the control system, which should control the inverter power designed in this work. The control must be capable for integrating the inverter using other obtainable RESs. The control approach plays a significant role in making the system smart via coordinating using IT systems like Internet synchronization Ether CAT networks. The second vital function is the inverter prototype. Then, the simulation of inverter power phase is obtained, and the subsequent step is the prototype execution. Thus, with the aid of lab view, it may be performed on real-time environment for performance. In engineering work, standard values are required to suit a definite work environment. Selection or design of HF transformers and IGBT/MOSFET switches using driver circuits is indispensable.

DATA AVAILABILITY STATEMENT

Data sharing is not applicable to this article as no new data were created or analyzed in this study.

ORCID

Suganthi Ramasamy https://orcid.org/0000-0003-4588-9627

REFERENCES

1. Ahmad Z, Singh SN. Comparative analysis of single phase transformerless inverter topologies for grid connected PV system. *Sol Energy*. 2017;149:245-271.
2. Shayestegan M, Shakeri M, Abunima H, et al. An overview on prospects of new generation single-phase transformerless inverters for grid-connected photovoltaic (PV) systems. *Renewable Sustainable Energy Rev*. 2018;82:515-530.
3. Mythili S, Thiyagarajah K, Rajesh P, Shajin FH. Ideal position and size selection of unified power flow controllers (UPFCs) to upgrade the dynamic stability of systems: an antlionoptimiser and invasive weed optimisation algorithm. *HKIE Trans*. 2020;27(1):25-37.
4. Ardashir JF, Sabahi M, Hosseini SH, Blaabjerg F, Babaei E, Gharehpetian GB. A single-phase transformerless inverter with charge pump circuit concept for grid-tied PV applications. *IEEE Trans Ind Electron*. 2016;64(7):5403-5415.
5. Guo X, Zhang X, Guan H, Kerekes T, Blaabjerg F. Three-phase ZVR topology and modulation strategy for transformerless PV system. *IEEE Trans Power Electron*. 2018;34(2):1017-1021.
6. Premkumar M, Sumithira TR. Design and implementation of new topology for solar PV based transformerless forward microinverter. *J Electr Eng Technol*. 2019;14(1):145-155.
7. Shayestegan M. Overview of grid-connected two-stage transformer-less inverter design. *J Mod Power Syst Clean Energy*. 2018;6(4):642-655.
8. Guo X, Jia X. Hardware-based cascaded topology and modulation strategy with leakage current reduction for transformerless PV systems. *IEEE Trans Ind Electron*. 2016;63(12):7823-7832.
9. Dutta S, Debnath D, Chatterjee K. A grid-connected single-phase transformerless inverter controlling two solar PV arrays

operating under different atmospheric conditions. *IEEE Trans Ind Electron*. 2017;65(1):374-385.
10. Rajeev M, Agarwal V. Single phase current source inverter with multiloop control for transformerless grid–PV interface. *IEEE Trans Ind Appl*. 2018;54(3):2416-2424.
11. Madeti SR, Singh SN. Monitoring system for photovoltaic plants: a review. *Renewable Sustainable Energy Rev*. 2017;67:1180-1207.
12. Firman A, Toranzos V, Vera L, Busso A, De La Casa J. Passive monitoring of the power generated in grid connected PV systems. *Energy Procedia*. 2014;57:235-244.
13. Ahmad Z, Singh SN. Single phase transformerless inverter topology with reduced leakage current for grid connected photovoltaic system. *Electr Power Syst Res*. 2018;154:193-203.
14. Rahimi R, Farhadi M, Moradi GR, Farhangi B, Farhangi S. Three-phase filter-clamped Transformerless inverter for grid-connected photovoltaic systems with low leakage current. *IEEE Trans Ind Appl*. 2020. https://doi.org/10.1109/TIA.2020.3008134.
15. Palanisamy R, Vijayakumar K. Transformerless three phase Z-source four wire voltage source inverter fed grid connected PV system. *Int. J. Ambient Energy*. 2020. https://doi.org/10.1080/01430750.2020.1781688.
16. Zhu Y, Fei J. Adaptive global fast terminal sliding mode control of grid-connected photovoltaic system using fuzzy neural network approach. *IEEE Access*. 2017;5:9476-9484.
17. Satti MB, Hasan A. Direct model predictive control of novel h-bridge multilevel inverter based grid-connected photovoltaic system. *IEEE Access*. 2019;7:62750-62758.
18. Rahimi R, Farhangi S, Farhangi B, Moradi GR, Afshari E, Blaabjerg F. H8 inverter to reduce leakage current in transformerless three-phase grid-connected photovoltaic systems. *IEEE J Emerg Sel Top Power Electron*. 2017;6(2):910-918.
19. Anurag A, Deshmukh N, Maguluri A, Anand S. Integrated DC–DC converter based grid-connected transformerless photovoltaic inverter with extended input voltage range. *IEEE Trans Power Electron*. 2017;33(10):8322-8330.
20. Grigoletto FB. Five-level transformerless inverter for single-phase solar photovoltaic applications. *IEEE J Emerg Sel Top Power Electron*. 2019;8:3411-22.
21. Guo X. A novel CH5 inverter for single-phase transformerless photovoltaic system applications. *IEEE Trans Circuits Syst II: Express Briefs*. 2017;64(10):1197-1201.
22. López H, Rodríguez-Reséndiz J, Guo X, Vázquez N, Carrillo-Serrano RV. Transformerless common-mode current-source inverter grid-connected for PV applications. *IEEE Access*. 2018;6:62944-62953.
23. Tey KS, Mekhilef S. A reduced leakage current transformerless photovoltaic inverter. *Renewable Energy*. 2016;86:1103-1112.
24. Fazlali B, Adib E. Quasi-resonant DC-link transformer-less structures for grid-connected PV systems. *Int J Electr Power Energy Syst*. 2018;103:384-394.
25. Guo X, Zhou J, He R, Jia X, Rojas CA. Leakage current attenuation of a three-phase cascaded inverter for transformerless grid-connected PV systems. *IEEE Trans Ind Electron*. 2017;65(1):676-686.
26. Li H, Zeng Y, Zhang B, Zheng TQ, Hao R, Yang Z. An improved H5 topology with low common-mode current for transformerless PV grid-connected inverter. *IEEE Trans Power Electron*. 2018;34(2):1254-1265.
27. Oshaba AS, Ali ES, AbdElazim SM. MPPT control design of PV system supplied SRM using BAT search algorithm. *Sustainable Energy Grids Networks*. 2015;2:51-60.
28. Jana KC, Biswas S, KarChaudhary S. Dual reference phase shifted PWM technique for a N-level inverter based grid connected solar photovoltaic system. *IET Renewable Power Gener*. 2016;10(7):928-935.
29. Ahmad Z, Singh SN. An improved single phase transformerless inverter topology for grid connected PV system with reduce leakage current and reactive power capability. *Sol Energy*. 2017;157:133-146.
30. Kadam A, Shukla A. A multilevel transformerless inverter employing ground connection between PV negative terminal and grid neutral point. *IEEE Trans Ind Electron*. 2017;64(11):8897-8907.
31. Mahmoudian M, Rodrigues EMG, Pouresmaeil E. An efficient H7 single-phase photovoltaic grid connected inverter for CMC conceptualization and mitigation method. *Electronics*. 2020;9(9):1440.
32. Meraj M, Rahman S, Iqbal A, Ben-Brahim L. Common mode voltage reduction in a single-phase quasi Z-source inverter for transformerless grid-connected solar PV applications. *IEEE J Emerg Sel Top Power Electron*. 2018;7(2):1352-1363.
33. Jedtberg H, Pigazo A, Liserre M, Buticchi G. Analysis of the robustness of transformerless PV inverter topologies to the choice of power devices. *IEEE Trans Power Electron*. 2016;32(7):5248-5257.
34. Lemley J, Bazrafkan S, Corcoran P. Deep Learning for Consumer Devices and Services: pushing the limits for machine learning, artificial intelligence, and computer vision. *IEEE Consum Electron Mag*. 2017;6(2):48-56.
35. Dey D, Chaudhuri S, Munshi S. Obstructive sleep apnoea detection using convolutional neural network based deep learning framework. *Biomed Eng Lett*. 2018;8(1):95-100.
36. Dey D, Chatterjee B, Dalai S, Munshi S, Chakravorti S. A deep learning framework using convolution neural network for classification of impulse fault patterns in transformers with increased accuracy. *IEEE Trans Dielectr Electr Insul*. 2017;24(6):3894-3897.
37. Wang S, Chen H. A novel deep learning method for the classification of power quality disturbances using deep convolutional neural network. *Appl Energy*. 2019;235:1126-1140.
38. Khan MA, Haque A, Kurukuru VB. Intelligent control of a novel transformerless inverter topology for photovoltaic applications. *Electr Eng*. 2019;102:1-5.
39. Kumar N, Saha TK, Dey J. Multilevel inverter (MLI)-based stand-alone photovoltaic system: modeling, analysis, and control. *IEEE Syst J*. 2019;14(1):909-915.

How to cite this article: Ramasamy S, Perumal M. CNN-based deep learning technique for improved H7 TLI with grid-connected photovoltaic systems. *Int J Energy Res*. 2021;45(14):19851-19868. doi:10.1002/er.7030